T-Hy-Demosaicing: Hyperspectral Reconstruction Via Tensor Subspace Representation Under Orthogonal Transformation

Shan-Shan Xu, Ting-Zhu Huang 🆔, Jie Lin 🆔, and Yong Chen 🆔

Abstract—This article aims to solve the problem of the hyperspectral imagery (HSI) demosaicing under a novel subsampling hyperspectral sensing strategy. The existing method utilizes the periodic structure of subsampling to estimate a fixed subspace in matrix form from the measurement result, which reduces the representation ability of the subspace in iterations and destroys the intrinsic structure of the tensor. To overcome these drawbacks, we propose a tensor-based HSI demosaicing (T-Hy-demosaicing) model with tensor subspace representation, which takes the low-tubal-rankness and the nonlocal self-similarity into account. In particular, we suggest a tensor singular value decomposition based on orthogonal transformation (Tran-based t-SVD) to learn the tensor subspace that possesses a more powerful representation ability. In addition, we develop an effective algorithm to solve the proposed nonconvex model under the framework of the proximal alternating minimization algorithm. Experiments conducted on simulated datasets illustrate that the proposed method outperforms other comparative methods in both visual and quantitative terms.

Index Terms—Hyperspectral demosaicing, proximal alternating minimization (PAM), tensor subspace representation, tran-based tensor singular value decomposition (t-SVD).

I. INTRODUCTION

HYPERSPECTRAL imagery (HSI) is a third-order tensor containing both spectral and spatial information. HSI consists of a great amount of bands, each of which represents the intensity of reflections measured over a narrow range of optical frequencies. Due to the high spectral resolution of the HSI, HSI can be widely used in environmental surveillance, military surveillance, medical detection, and agricultural planning, etc. [1]–[10]. However, higher spectral resolution means larger volume, which will greatly increase the burden of transmission

and storage. To avoid these problems, HSI is usually compressed before transmission in actual situations. Therefore, The choice of compression method and HSI reconstruction from compressed observations (even with noise) are crucial for subsequent applications [11]–[15].

According to the difference in compressed direction, compression methods can be classified into three categories: 1) Spatial-based methods. 2) Spatial-Spectral-based methods. 3) Spectral-based methods. The Spatial-based methods convert the image of each band to a sparse domain, and then perform a down-sampling band-by-band [16]–[18]. These methods are only a simple extension of the compressed sensing methods of 2-D images, which cannot make full advantage of the spectral information of the HSI and cause a heavier burden on hardware devices and sensor resources. To joint utilizes the spatial and spectral information, spatial-spectral-based methods, which perform separable compression in multiple directions, were proposed in [19]–[22]. Inevitably, this type of methods makes the sampling setup more complicated. Recently, many researchers have discovered that the spectral dimension of the HSI has better compressibility due to the higher correlation of this dimension. Therefore, the spectral-based methods are widely used, and its compression process can be described as making a random projection for every spectral vector [23]–[26]. However, this kind of methods usually has a large-sized sensing matrice generated by random numbers or compressive operators satisfying the restricted isometry property [27], which will occupy large computing resources during the reconstruction process.

Recently, a novel and fast hyperspectral sensing framework called Hy-mosaicing was discussed by Zhuang *et al.* [28], which is inspired by the color filter array used in some digital cameras. It is worth mentioning that this sensing framework has a more special sensing matrix, which is a binary matrix composed of random row subsets of the identity matrix. It is very lightweight and can be better compatible with the constraints imposed by the hardware that collects HSI information. Meanwhile, the sensing framework has a periodic sampling structure, as shown in Fig. 2, which means that there exist a number of pixels sharing the same sensing matrix. This implies that the complexity of sampling can be reduced. Under this framework, they proposed a subspace-based blind reconstruction method called Hy-demosaicing using the low-rankness and self-similarity of HSI. According to the periodic structure of the color selector
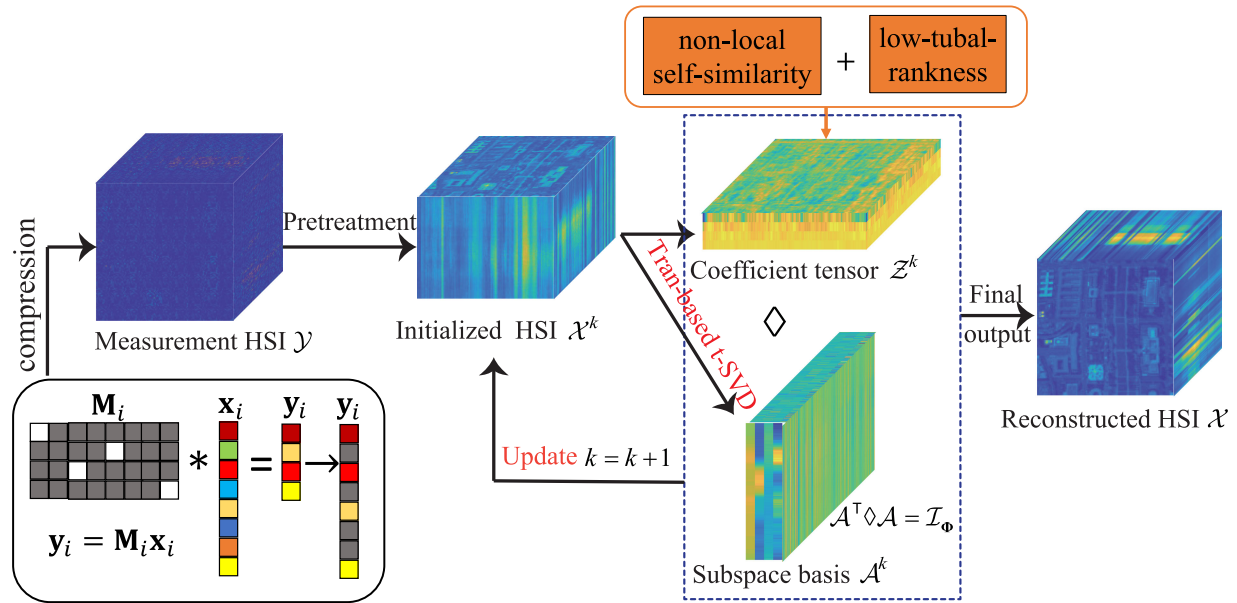
Fig. 1. Flow diagram of the proposed T-Hy-demosaicing method for HSI demosaicing.
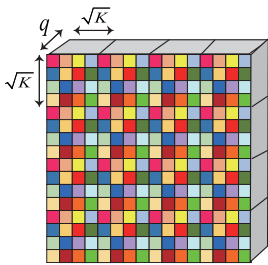

Fig. 2. Sampling structure.

array, this method can get subspace basis from the measured subsamples, and the solution is more efficient. However, this method also has some disadvantages: The model expands the HSI data into a 2-D matrix for processing, which cannot finely preserve the tensor intact of the HSI. Moreover, Hy-mosaicing method fixed the subspace matrix and cannot be self-updated. It can be seen that the method Hy-demosaicing still has room for improvement, and the most essential issue is how to construct a subspace representation in the form of tensor.

In essence, the HSI is a natural tensor and has a high correlation in both spatial and spectral dimensions [29]–[34]. This implies the low-rankness of the HSI tensor and the entire tensor corresponds to the affiliation of a tensor subspace. Finding a proper tensor decomposition with a specific rank measure, the HSI tensor is expected to be faithfully represented by a tensor subspace. Recently, Kilmer *et al.* [35] proposed a novel tensor singular value decomposition (t-SVD) and tensor–tensor multiplication (t-product), which uses discrete fourier transform (DFT) to decompose a tensor into the t-product of three tensors. However, DFT is not necessarily applicable to all types of data. Is it possible to construct a framework that can make the decomposition performance of t-SVD more flexible and deeper

to preserve the original data information when on different data? To track this problem, we suggest a t-SVD based on orthogonal transformation (Tran-Based t-SVD) (see Section IV-C2).

In this article, we propose a T-Hy-demosaicing method. The flowchart of the proposed method is shown in Fig. 1. Our main contributions are as follows.

1) We design a tensor subspace representation and propose a T-Hy-demosaicing method for HSI demosaicing. Under the tensor subspace representation framework, the reconstruction problem of the observation is transformed into the estimation of the coefficient tensor, and the coefficient tensor is achieved by nonlocal-based denoiser.

2) We suggest a t-SVD based on orthogonal transformation to learn tensor subspace. With the new decomposition, the transformation can be chosen more flexibly for our demosaicing problem, and the learned subspace has stronger representation capability.

3) We use the proximal alternating minimization (PAM) algorithm to efficiently solve the proposed nonconvex model. Extensive experiments indicate that the proposed algorithm has better results in both visual and quantitative evaluation than existing methods.

The remainder of this article is organized as follows. Section II introduces the basic notations and basic definitions of third-order tensor, as well as a hyperspectral sensing framework (mosaic of HSI). Section III proposes the model and algorithm. Section IV gives the experimental results and analyzes the superiority of the algorithm proposed. The final conclusions are given in Section V. The proof is in the Appendix.

II. PRELIMINARIES AND PROBLEM BACKGROUND

We first give some notations used frequently in this article. We denote vectors by boldface lowercase letters, e.g., $\mathbf{a}$. Matrices

are denoted by boldface capital letters, e.g., $\mathbf{A}$, and tensors are denoted by boldface Euler script letters, e.g., $\mathcal{A}$. The fields of real number and complex number are denoted as $\mathbb{R}$ and $\mathbb{C}$. For a third-order tensor $\mathcal{A} \in \mathbb{R}^{n_1 \times n_2 \times n_3}$, we denote $\mathcal{A}^{(k)}$ as the kth frontal slice of $\mathcal{A}$, $\mathcal{A}(i,j,:)$ as its tubal obtained by fixing the first two dimensions and varying the third dimension, and $\mathcal{A}_{ijk}$ as its (i,j,k) th entry and its Frobenius norm is $\|\mathcal{A}\|_F = \sqrt{\sum_{ijk} \mathcal{A}_{ijk}^2}$.

A. Framework of the t-SVD With Orthogonal Transformation

Different from using DFT matrix to define t-product and t-SVD in [35], we develop a novel tensor t-SVD based on orthogonal transformation [36], [37].

For any third-order tensor $\mathcal{X} \in \mathbb{C}^{n_1 \times n_2 \times n_3}$, $\bar{\mathcal{X}}_{\boldsymbol{\Phi}}$ is a third-order tensor, which is obtained via multiplying by $\boldsymbol{\Phi}$ on each tube along the third-dimension of $\mathcal{X}$

$$\bar{\mathcal{X}}_{\boldsymbol{\Phi}}(i,j,:) = \boldsymbol{\Phi} \cdot (\mathcal{X}(i,j,:))$$

where $\boldsymbol{\Phi} \in \mathbb{C}^{n_3 \times n_3}$ is an orthogonal transformation matrix with $\boldsymbol{\Phi}\boldsymbol{\Phi}^{\mathsf{T}} = \boldsymbol{\Phi}^{\mathsf{T}}\boldsymbol{\Phi} = \mathbf{I}$, and $\mathbf{I} \in \mathbb{C}^{n_3 \times n_3}$ is an identity matrix. Obviously, we can get $\mathcal{X}$ by multiplying $\boldsymbol{\Phi}^{\mathsf{T}}$ along each tube of $\bar{\mathcal{X}}_{\boldsymbol{\Phi}}$, i.e., $\mathcal{X} = \boldsymbol{\Phi}^{\mathsf{T}}[\bar{\mathcal{X}}_{\boldsymbol{\Phi}}]$, which is a reversible operation.

We use the frontal slices of $\bar{\mathcal{X}}_{\boldsymbol{\Phi}}$ to construct a block diagonal matrix as follows:

$$\mathrm{bdiag}\left(\bar{\mathcal{X}}_{\boldsymbol{\Phi}}\right) := \begin{pmatrix} \bar{\mathcal{X}}_{\boldsymbol{\Phi}}^{(1)} & & & \\ & \bar{\mathcal{X}}_{\boldsymbol{\Phi}}^{(2)} & & \\ & & \ddots & \\ & & & \bar{\mathcal{X}}_{\boldsymbol{\Phi}}^{(n_3)} \end{pmatrix}$$

where bdiag is the operator that maps the tensor to a block diagonal matrix. Moreover, we can convert the block diagonal matrix to a tensor through the following fold operator:

$$\mathrm{fold}\left(\mathrm{bdiag}\left(\bar{\mathcal{X}}_{\boldsymbol{\Phi}}\right)\right) = \bar{\mathcal{X}}_{\boldsymbol{\Phi}}$$

Definition 1 (Tran-based t-product [36]): Set $\mathcal{X} \in \mathbb{C}^{n_1 \times n_2 \times n_3}$ and $\mathcal{Y} \in \mathbb{C}^{n_2 \times l \times n_3}$, then the Tran-based t-product is defined as

$$\mathcal{C} = \mathcal{X} \diamond \mathcal{Y} = \boldsymbol{\Phi}^{\mathsf{T}}\left[\mathrm{fold}\left(\mathrm{bdiag}\left(\bar{\mathcal{X}}_{\boldsymbol{\Phi}}\right) \cdot \mathrm{bdiag}\left(\bar{\mathcal{Y}}_{\boldsymbol{\Phi}}\right)\right)\right] \quad (1)$$

where $\mathcal{C} \in \mathbb{C}^{n_1 \times l \times n_3}$.

Definition 2 (Tensor transpose [36]): The transpose of $\mathcal{X} \in \mathbb{C}^{n_1 \times n_2 \times n_3}$ is denoted as $\mathcal{X}^{\mathsf{T}} \in \mathbb{C}^{n_2 \times n_1 \times n_3}$, which satisfies $(\bar{\mathcal{X}}_{\boldsymbol{\Phi}}^{\mathsf{T}})^{(i)} = (\bar{\mathcal{X}}_{\boldsymbol{\Phi}}^{(i)})^{\mathsf{T}}, i = 1, \ldots, n_3$.

Definition 3 (Identity tensor [36]): Let $\mathcal{I} \in \mathbb{R}^{n \times n \times n_3}$ is a tensor, whose each frontal slice is a $n \times n$ identity matrix. Then $\mathcal{I}_{\boldsymbol{\Phi}} = \boldsymbol{\Phi}^{\mathsf{T}}[\mathcal{I}]$ is called the identity tensor.

Definition 4 (Orthogonal tensor [36]): A tensor $\mathcal{Q} \in \mathbb{C}^{n \times n \times n_3}$ is orthogonal if it has

$$\mathcal{Q}^{\mathsf{T}} \diamond \mathcal{Q} = \mathcal{Q} \diamond \mathcal{Q}^{\mathsf{T}} = \mathcal{I}_{\boldsymbol{\Phi}}$$

where $\mathcal{I}_{\boldsymbol{\Phi}}$ is an identity tensor.

Based on the above t-product, the corresponding t-SVD can be defined as follows.

Definition 5 (Tran-based t-SVD [36]): For any third-order tensor $\mathcal{X} \in \mathbb{C}^{n_1 \times n_2 \times n_3}$, its Tran-based t-SVD is defined as

$$\mathcal{X} = \mathcal{U} \diamond \mathcal{S} \diamond \mathcal{V}^{\mathsf{T}}$$

where $\mathcal{U} \in \mathbb{C}^{n_1 \times n_1 \times n_3}$ and $\mathcal{V} \in \mathbb{C}^{n_2 \times n_2 \times n_3}$ are third-order orthogonal tensors with respect to the Tran-based t-product, $\mathcal{S} \in \mathbb{C}^{n_1 \times n_2 \times n_3}$ is f-diagonal tensor whose frontal slices are diagonal matrices, and $\mathcal{V}^{\mathsf{T}}$ is the tensor transpose of $\mathcal{V}$.

Definition 6 (Tensor tubal rank [36]): For any third-order tensor $\mathcal{X} \in \mathbb{C}^{n_1 \times n_2 \times n_3}$, the tensor tubal rank of $\mathcal{X}$, denoted as $\mathrm{rank}_t(\mathcal{X})$, is defined as the number of nonzero singular tubes of $\mathcal{S}$, i.e.,

$$\mathrm{rank}_t(\mathcal{X}) = \#\{i, \mathcal{S}(i,i,:) \neq 0\}$$

where $\mathcal{S}$ is from the Tran-based t-SVD of $\mathcal{X} = \mathcal{U} \diamond \mathcal{S} \diamond \mathcal{V}^{\mathsf{T}}$.

Remark 1: The above definitions are applicable to any orthogonal transformation, but for different problems, it is particularly important to choose a suitable orthogonal transformation matrix. For the following reasons, the demosaicing problem for this article is to employ the tensor decomposition and product based on the discrete cosine transform (DCT). First, for the compression problem, DCT can retain the most relevant information (low-frequency information) of HSI. Second, DCT uses the intrinsic reflexive boundary conditions along the mode-3 of the tensor, which has a better reconstruction effect at the image boundary. Finally, DCT does not involve the calculation of the complex part, theoretically speaking, it can reduce a certain calculation cost.

B. Sampling Strategy: Hy-Mosaicing

Based on the color filter array used in color images, our hyperspectral sensing strategy is to randomly select samples in the spectral dimension as measurement data for each pixel in the spatial dimension. The subsampling process of the ith pixel $\mathbf{x}_i \in \mathbb{R}^b$ can be described in the following mathematical form:

$$\mathbf{y}_i = \mathbf{M}_i \mathbf{x}_i \quad (2)$$

where $\mathbf{y}_i \in \mathbb{R}^q (q \ll b)$ is measured vector, and $\mathbf{M}_i \in \mathbb{R}^{q \times b}$ is the measurement matrix used for color subsampling. It is a binary matrix consisting of a random row subset of the identity matrix. However, we do not use a different measurement matrix for each pixel in space. We divide the HSI into several nonoverlapping square windows of size K in the spatial dimension, and then generate a color selector array of size K, each pixel of which corresponds to a different measurement matrix (color). Finally, we copy the color pattern in the unit of size K to generate our measurement matrix. The sampling structure is shown in Fig. 2.

To better maintain the structure of HSI, the HSI is expressed as a third-order tensor. Assuming that $\mathcal{X} \in \mathbb{R}^{m \times n \times b}$ is the clean HSI, when it is contaminated by the additive Gaussian noise $\mathcal{N} \in \mathbb{R}^{m \times n \times b}$, then the noisy HSI $\mathcal{Y} \in \mathbb{R}^{m \times n \times b}$ is formulated as

$$\mathcal{Y} = \mathcal{X} + \mathcal{N}. \quad (3)$$

We perform subsampling on each pixel in $\mathcal{X}$ as (2). Under the condition of knowing the mask corresponding to each pixel, we

$$
\begin{bmatrix} 0 & 0 & 0 & 1 & 0 & 0 & 0 \\ 1 & 0 & 0 & 0 & 0 & 0 & 0 \\ 0 & 0 & 1 & 0 & 0 & 0 & 0 \end{bmatrix} * \begin{bmatrix} x_{i1} \\ x_{i2} \\ x_{i3} \\ x_{i4} \\ x_{i5} \\ x_{i6} \\ x_{i7} \end{bmatrix} \rightarrow \begin{bmatrix} x_{i4} \\ x_{i1} \\ x_{i3} \\ y_i \end{bmatrix}
$$

$$M_i \qquad\qquad x_i$$

Matrix form

$$
\Rightarrow \begin{bmatrix} 1 & 0 & 1 & 1 & 0 & 0 & 0 \end{bmatrix}^{\mathsf{T}} \odot \begin{bmatrix} x_{i1} \\ x_{i2} \\ x_{i3} \\ x_{i4} \\ x_{i5} \\ x_{i6} \\ x_{i7} \end{bmatrix} \rightarrow \begin{bmatrix} x_{i1} \\ 0 \\ x_{i3} \\ x_{i4} \\ 0 \\ 0 \\ 0 \end{bmatrix}
$$

$$\mathcal{M}(j,k,:) \qquad\qquad \mathcal{X}(j,k,:) \quad \mathcal{Y}(j,k,:)$$

Tensor form

Fig. 3. Mask matrix to tensor.

can fill in the unsampled position of the measured vector with 0. Then, the sensing process can be formulated as

$$\mathcal{Y} = \mathcal{M} \odot \mathcal{X} + \mathcal{N} \tag{4}$$

where $\mathcal{M} \in \mathbb{R}^{m \times n \times b}$ is a binary tensor that can be obtained from the $\mathbf{M}_i$ of each pixel and $\odot$ denotes the Hadamard (entrywise) product. In each tube of $\mathcal{M}$, there is $\sum \mathcal{M}(i,j,:) = q$. The corresponding relationship between $\mathbf{M}_i$ and $\mathcal{M}$ is shown in Fig. 3. q/b stands for the sampling rate. Moreover, we mainly consider the reconstruction of the HSI in this article. The pixel values of the image are scaled and usually belong to the interval [0 255].

III. DEMOSAICING: THE PROPOSED MODEL AND THE PAM ALGORITHM

In this section, under the abovementioned sampling strategy called Hy-mosaicing, we propose an HSI demosaicing model based on tensor subspace representation and develop an effective algorithm to solve it under the framework of the PAM algorithm.

A. Proposed Model

Since it is an ill-posed issue to reconstruct $\mathcal{X}$ under the conditions of known $\mathcal{M}$ and $\mathcal{Y}$ in (4), and it is difficult to solve directly. Therefore, according to the special properties of HSI data, we can add some prior conditions [38]–[44]. Based on the new tensor decomposition, we represent an original tensor data as the Tran-based t-product of a tensor basis and a coefficient tensor. In particular, we found that the obtained coefficient tensor in the subspace can well inherit the nonlocal self-similarity of the original HSI, which can be well characterized by the $\|.\|_{\mathrm{NL}}$ regularity, as shown in Fig. 4. From the above, the proposed HSI demosaicing model by tensor factorization with a nonlocal
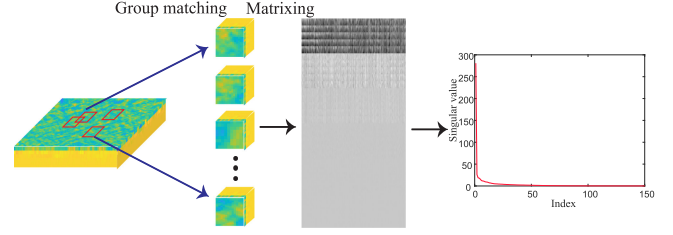

Fig. 4. Nonlocal self-similarity property of coefficient tensor.

low-rank regularizer is described as follows:

$$\min_{\mathcal{Z},\mathcal{A},\mathcal{X}} \frac{1}{2}\|\mathcal{M}\odot\mathcal{X}-\mathcal{Y}\|_F^2 + \lambda_1\|\mathcal{X}-\mathcal{A}\diamond\mathcal{Z}\|_F^2 + \lambda_2\|\mathcal{Z}\|_{\mathrm{NL}}$$

$$\text{such that } \mathcal{A}^{\mathsf{T}}\diamond\mathcal{A}=\mathcal{I}_{\Phi} \tag{5}$$

where $\mathcal{A}$ is a semi-orthogonal basis tensor with respect to an orthogonal transformation matrix Φ, which captures the common subspace of different spectrums, and $\mathcal{Z}$ is the coefficient tensor. Since the permuted HSI has better low-tubal-rank property than the original data, we all perform permutation operations for $\mathcal{M}$, $\mathcal{X}$, and $\mathcal{Y}$, so that $\mathcal{M},\mathcal{X},\mathcal{Y}\in\mathbb{R}^{b\times m\times n}$. It is assumed that there is an optimal tubal rank $p\ll b$ such that $\mathcal{X}$ can be decomposed into subspaces with the size of p, then $\mathcal{A}\in\mathbb{R}^{b\times p\times n}$, $\mathcal{Z}\in\mathbb{R}^{p\times m\times n}$.

B. PAM Algorithm

Since (5) is nonconvex, we develop the PAM algorithm to solve it efficiently, which can guarantee numerical stability, see, e.g., [45], [46]. Therefore, the solution of model (5) is to split the original problem into three subproblems and solve them alternately. Given an initial guess $(\mathcal{X}^k,\mathcal{A}^k,\mathcal{Z}^k)$ for the problem (5), the PAM iteration steps are as follows:

$$
\begin{cases}
\mathcal{Z}^{k+1} = \arg\min_{\mathcal{Z}} \lambda_1\left\|\mathcal{X}^k-\mathcal{A}^k\diamond\mathcal{Z}\right\|_F^2 + \lambda_2\|\mathcal{Z}\|_{\mathrm{NL}} \\
\qquad\qquad + \rho\left\|\mathcal{Z}-\mathcal{Z}^k\right\|_F^2 \\
\mathcal{A}^{k+1} = \arg\min_{\mathcal{A}^{\mathsf{T}}\diamond\mathcal{A}=\mathcal{I}_{\Phi}} \lambda_2\left\|\mathcal{X}^k-\mathcal{A}\diamond\mathcal{Z}^{k+1}\right\|_F^2 + \rho\left\|\mathcal{A}-\mathcal{A}^k\right\|_F^2 \\
\mathcal{X}^{k+1} = \arg\min_{\mathcal{X}} \frac{1}{2}\|\mathcal{M}\odot\mathcal{X}-\mathcal{Y}\|_F^2 + \rho\left\|\mathcal{X}-\mathcal{X}^k\right\|_F^2 \\
\qquad\qquad + \lambda_1\left\|\mathcal{X}-\mathcal{A}^{k+1}\diamond\mathcal{Z}^{k+1}\right\|_F^2.
\end{cases}
$$

1) $\mathcal{Z}$ Subproblem: $\mathcal{Z}$ subproblem is formulated as follows:

$$\mathcal{Z}^{k+1} = \arg\min_{\mathcal{Z}} \lambda_1\left\|\mathcal{X}^k-\mathcal{A}^k\diamond\mathcal{Z}\right\|_F^2 + \lambda_2\|\mathcal{Z}\|_{\mathrm{NL}}$$

$$+ \rho\left\|\mathcal{Z}-\mathcal{Z}^k\right\|_F^2$$

$$= \arg\min_{\mathcal{Z}} \lambda_1\left\|(\mathcal{A}^k)^{\mathsf{T}}\diamond\mathcal{X}^k-\mathcal{Z}\right\|_F^2 + \lambda_2\|\mathcal{Z}\|_{\mathrm{NL}}$$

$$+ \rho\left\|\mathcal{Z}-\mathcal{Z}^k\right\|_F^2 \tag{6}$$

$$= \arg\min_{\mathcal{Z}} \frac{\lambda_1+\rho}{\lambda_2}\left\|\mathcal{Z}-\frac{\lambda_1(A^k)^{\mathsf{T}}\diamond\mathcal{X}^k+\rho\mathcal{Z}^k}{\lambda_1+\rho}\right\|_F^2$$

$$+ \|\mathcal{Z}\|_{NL}.$$

TABLE I
VALUE OF THE SUBSPACE DIMENSION p UNDER DIFFERENT SPECTRAL SAMPLING NUMBERS q AND NOISE LEVELS

Spectral sample number q	$4 \leq q < 10$	$10 \leq q < 20$	$20 \leq q < 30$	$30 \leq q < 40$	$40 \leq q < 60$	$60 \leq q < 100$
SNR=20 dB	3	4	4	5	7	8
SNR=30 dB	3	4	4	6	7	9
SNR=40 dB	4	5	6	7	8	10

Regarding the derivation of (6), we need to prove that the following equation holds:

$$\underset{\mathcal{Z}}{\arg\min} \, \lambda_1 \big\| \mathcal{X}^k - \mathcal{A}^k \diamond \mathcal{Z} \big\|_F^2$$
$$= \underset{\mathcal{Z}}{\arg\min} \, \lambda_1 \big\| (\mathcal{A}^k)^\mathsf{T} \diamond \mathcal{X}^k - \mathcal{Z} \big\|_F^2. \tag{7}$$

We perform a specific orthogonal transformation along the mode-3 for all variables in (7), each frontal slice of them can be written as

$$\underset{\bar{\mathbf{Z}}^{(i)}}{\arg\min} \, \lambda_1 \big\| \bar{\mathbf{X}}^{(i)} - \bar{\mathbf{A}}^{(i)} \bar{\mathbf{Z}}^{(i)} \big\|_F^2$$
$$= \underset{\bar{\mathbf{Z}}^{(i)}}{\arg\min} \, \lambda_1 \big\| (\bar{\mathbf{A}}^{(i)})^\mathsf{T} \bar{\mathbf{X}}^{(i)} - \bar{\mathbf{Z}}^{(i)} \big\|_F^2$$

then (7) is valid combined with the following Theorem 1. This problem can be solved by the state-of-the-art plug-and-play (PnP) denoiser (such as WNNM method, BM3D method, etc.), see [47]–[50] for their specific solution process.

Theorem 1: Let $\mathbf{A}$ be a semiorthogonal matrix, i.e. $\mathbf{A}^\mathsf{T}\mathbf{A} = \mathbf{I}$, where $\mathbf{I}$ is the identity matrix. Then,

$$\underset{\mathbf{Z}}{\arg\min} \, \|\mathbf{X} - \mathbf{A}\mathbf{Z}\|_F^2 = \underset{\mathbf{Z}}{\arg\min} \, \big\| \mathbf{A}^\mathsf{T}\mathbf{X} - \mathbf{Z} \big\|_F^2.$$

2) $\mathcal{A}$ Sub-Problem: $\mathcal{A}$ sub-problem is formulated as follows:

$$\mathcal{A}^{k+1} = \underset{\mathcal{A}^\mathsf{T} \diamond \mathcal{A} = \mathcal{I}_\Phi}{\arg\min} \, \lambda_2 \big\| \mathcal{X}^k - \mathcal{A} \diamond \mathcal{Z}^{k+1} \big\|_F^2 + \rho \big\| \mathcal{A} - \mathcal{A}^k \big\|_F^2. \tag{8}$$

According to Theorem 2, the closed-form solution of $\mathcal{A}$ is given as

$$\mathcal{A}^{k+1} = \mathcal{V} \diamond \mathcal{U}^\mathsf{T} \tag{9}$$

where $\mathcal{U}$ and $\mathcal{V}$ are obtained by performing Tran-based t-SVD of $\lambda_2 \mathcal{Z}^{k+1} \diamond \mathcal{X}^\mathsf{T} + \rho \mathcal{A}^{k\mathsf{T}}$, that is, $\lambda_2 \mathcal{Z}^{k+1} \diamond \mathcal{X}^\mathsf{T} + \rho \mathcal{A}^{k\mathsf{T}} = \mathcal{U} \diamond \mathcal{S} \diamond \mathcal{V}^\mathsf{T}$.

Theorem 2 ([51]): For a semiorthogonal tensor $\mathcal{A} \in \mathbb{R}^{n_1 \times n_2 \times n_3}$, the following problem:

$$\underset{\mathcal{A}}{\min} \, \lambda_2 \|\mathcal{X} - \mathcal{A} \diamond \mathcal{Z}\|_F^2 + \rho \|\mathcal{A} - \mathcal{B}\|_F^2, \text{ s.t. } \mathcal{A}^\mathsf{T} \diamond \mathcal{A} = \mathcal{I}_\Phi \tag{10}$$

has the closed-form solution $\mathcal{A}^* = \mathcal{V} \diamond \mathcal{U}^\mathsf{T}$, where $\mathcal{U}$ and $\mathcal{V}$ are obtained by performing Tran-based t-SVD of $\lambda_2 \mathcal{Z} \diamond \mathcal{X}^\mathsf{T} + \rho \mathcal{B}^\mathsf{T}$, that is, $\lambda_2 \mathcal{Z} \diamond \mathcal{X}^\mathsf{T} + \rho \mathcal{B}^\mathsf{T} = \mathcal{U} \diamond \mathcal{S} \diamond \mathcal{V}^\mathsf{T}$.

3) $\mathcal{X}$ Subproblem: $\mathcal{X}$ subproblem is formulated as follows:

$$\mathcal{X}^{k+1} = \underset{\mathcal{X}}{\arg\min} \, \frac{1}{2}\|\mathcal{M} \odot \mathcal{X} - \mathcal{Y}\|_F^2 + \rho\|\mathcal{X} - \mathcal{X}^k\|_F^2$$
$$+ \lambda_1 \|\mathcal{X} - \mathcal{A}^{k+1} \diamond \mathcal{Z}^{k+1}\|_F^2. \tag{11}$$

Let $\mathcal{J} = \frac{1}{2}\|\mathcal{M} \odot \mathcal{X} - \mathcal{Y}\|_F^2 + \lambda_1\|\mathcal{X} - \mathcal{A}^{k+1} \diamond \mathcal{Z}^{k+1}\|_F^2 + \rho\|\mathcal{X} - \mathcal{X}^k\|_F^2$, we have the partial derivative of $\mathcal{J}$ with respect

TABLE II
CRITICAL PARAMETERS OF COMPARED METHODS

Methods	Parameters
HaLRTC	$\lambda \in \{10^{-3}, 10^{-2}, 10^{-1}\}$
LRTC-TV-I	$\beta \in \{[1, 1, 1], [1, 1, 0]\}$, $\lambda = 0.02$, $\rho = 10^{-2}$
TNN	$\lambda \in \{10^{-3}, 10^{-2}, 10^{-1}\}$
KBR	$\beta = 10^{-2}$, $\mu \in \{\beta \cdot 10^{-3}, \beta \cdot 10^{-4}, \beta \cdot 10^{-5}\}$
Hy-demosaicing	$p\_subspace \in \{2 : 6\}$, $\lambda \in \{0.02, 0.0075, 0.0025\}$

to $\mathcal{X}$ as

$$\frac{\partial \mathcal{J}}{\partial \mathcal{X}} = (\mathcal{M} + 2\lambda_1 + 2\rho) \odot \mathcal{X}$$
$$- (\mathcal{M} \odot \mathcal{Y} + 2\lambda_1 \mathcal{A}^{k+1} \diamond \mathcal{Z}^{k+1} + 2\rho \mathcal{X}^k).$$

Take $\frac{\partial \mathcal{J}}{\partial \mathcal{X}} = 0$, $\mathcal{X}$ can be given by

$$\mathcal{X}^{k+1} = (\mathcal{M} \odot \mathcal{Y} + 2\lambda_1 \mathcal{A}^{k+1} \diamond \mathcal{Z}^{k+1}$$
$$+ 2\rho \mathcal{X}^k) \oslash (\mathcal{M} + 2\lambda_1 + 2\rho). \tag{12}$$

In summary, we propose a new demosaicing algorithm for HSI as follows:

Algorithm 1: T-Hy-Demosaicing.

Input: Sampling mask $\mathcal{M}$, measurements $\mathcal{Y}$, a preprocessed HSI $\mathcal{X}^0$ using TNN method, parameters $\lambda_1, \lambda_2, p, \rho$.
1: Initialize: Estimate $\mathcal{A}^0$ and $\mathcal{Z}^0$ via Tran-based t-SVD on $\mathcal{X}^0$.
2: **for** $k = 1 : M$ **do**
3:     update $\mathcal{Z}$ via solving (6) with the PnP denoiser.
4:     update $\mathcal{A}$ via (9).
5:     update $\mathcal{X}$ via (12).
6:     **if** $\|\mathcal{X}^k - \mathcal{X}^{k-1}\|/\|\mathcal{X}^{k-1}\| \leq \epsilon$ **then**
7:         break.
8:     **end if**
9: **end for**
Output: Reconstructed HSI $\mathcal{X}$.

IV. EXPERIMENTAL RESULTS

In this section, to verify the effectiveness and superiority of the proposed method for the demosaicing problem, we conduct simulation experiments on real HSI data. Since the Hy-demosaicing problem can be regarded as a completion problem, the existing completion methods are also suitable for solving this problem. Thus, the compared methods include: HaLRTC [52], LRTC-TV-I [53], TNN [54], KBR [55], and Hy-demosaicing [28]. The experimental results are compared with these methods in terms of quantitative indices and visual effects.

TABLE III
QUANTITATIVE COMPARISON OF COMPARED METHODS ON SIMULATED DATA

Dataset	SNR	SR	Indices	Measurement	HaLRTC	LRTC-TV-I	TNN	KBR	Hy-demosaicing	T-Hy-demosaicing
WDC	20 dB	5%	MPSNR	13.090	15.628	20.626	24.620	**29.102**	25.088	29.055
			MSSIM	0.0302	0.2460	0.3707	0.7723	0.8606	0.7820	**0.8887**
			MSAM	77.167	29.993	13.668	16.079	**7.9639**	17.827	11.084
			NMSE	0.9485	0.5488	0.1545	0.0747	**0.0238**	0.0791	0.0299
		15%	MPSNR	13.436	21.117	24.237	32.131	35.516	34.278	**36.950**
			MSSIM	0.0662	0.5832	0.6340	0.9228	0.9596	0.9651	**0.9708**
			MSAM	69.638	15.201	10.193	7.9451	5.2850	7.0728	**4.8200**
			NMSE	0.8752	0.1577	0.0670	0.0112	0.0047	0.0069	**0.0034**
		25%	MPSNR	14.103	27.515	27.975	33.889	36.955	38.272	**40.693**
			MSSIM	0.1342	0.8349	0.8236	0.9418	0.9683	0.9852	**0.9867**
			MSAM	60.469	9.4814	8.2271	7.0589	5.0177	4.1904	**3.2242**
			NMSE	0.7508	0.0323	0.0283	0.0070	0.0033	0.0027	**0.0014**
		50%	MPSNR	15.855	31.944	31.936	34.537	36.484	41.217	**42.872**
			MSSIM	0.2897	0.9190	0.9247	0.9454	0.9629	**0.9916**	0.9916
			MSAM	45.625	7.4020	7.6535	6.9504	5.6542	2.6532	**2.5669**
			NMSE	0.4999	0.0108	0.0109	0.0057	0.0036	0.0015	**0.0009**
	30 dB	5%	MPSNR	13.092	15.659	20.692	25.105	**30.145**	25.379	29.819
			MSSIM	0.0305	0.2496	0.3804	0.7997	0.8894	0.7983	**0.9068**
			MSAM	77.012	29.622	13.478	15.122	**7.0781**	16.842	10.002
			NMSE	0.9482	0.5460	0.1524	0.0686	**0.0198**	0.0729	0.0258
		15%	MPSNR	13.441	21.322	24.446	35.200	40.623	34.716	**41.180**
			MSSIM	0.0672	0.5994	0.6568	0.9600	0.9852	0.9695	**0.9894**
			MSAM	69.379	14.603	9.5584	5.6348	3.4058	6.8363	**2.8823**
			NMSE	0.8745	0.1521	0.0643	0.0061	0.0014	0.0064	**0.0014**
		25%	MPSNR	14.114	28.469	28.550	38.985	42.245	38.947	**45.852**
			MSSIM	0.1367	0.8684	0.8522	0.9805	0.9896	0.9885	**0.9955**
			MSAM	60.073	8.2398	6.8505	3.9887	2.9020	3.9093	**1.8770**
			NMSE	0.7494	0.0267	0.0253	0.0025	0.0010	0.0024	**0.0005**
		50%	MPSNR	15.890	35.244	34.105	41.637	43.721	43.990	**49.417**
			MSSIM	0.2969	0.9678	0.9563	0.9883	0.9925	0.9960	**0.9979**
			MSAM	44.949	4.9287	4.7212	3.1301	2.4987	2.0769	**1.2728**
			NMSE	0.4972	0.0056	0.0069	0.0012	0.0007	0.0008	**0.0002**
PaU	20 dB	5%	MPSNR	13.556	14.283	20.799	27.186	28.863	24.557	**30.318**
			MSSIM	0.0253	0.0857	0.3120	0.7927	0.8416	0.7473	**0.8761**
			MSAM	77.683	53.031	9.9434	12.420	**8.5601**	16.944	10.785
			NMSE	0.9512	0.8119	0.1774	0.0443	0.0274	0.1072	**0.0235**
		15%	MPSNR	14.034	23.959	25.814	31.511	35.120	35.702	**36.406**
			MSSIM	0.0686	0.6256	0.7018	0.8986	0.9517	**0.9624**	0.9589
			MSAM	67.961	10.813	8.5187	10.351	7.2978	**6.0594**	6.9518
			NMSE	0.8507	0.0848	0.0542	0.01727	0.0061	0.0061	**0.0055**
		25%	MPSNR	14.571	27.048	28.973	32.996	35.084	39.005	**39.485**
			MSSIM	0.1166	0.7888	0.8469	0.9202	0.9495	**0.9819**	0.9805
			MSAM	61.027	9.8616	8.2011	9.6656	7.8816	**4.3833**	4.7917
			NMSE	0.7517	0.0411	0.0257	0.0117	0.0061	0.0027	**0.0024**
		50%	MPSNR	16.307	31.634	32.790	34.090	36.049	40.499	**41.325**
			MSSIM	0.2549	0.9097	0.9258	0.9340	0.9576	0.9845	**0.9866**
			MSAM	46.644	8.9997	8.4418	9.2402	7.5086	**3.7111**	4.1588
			NMSE	0.5032	0.0138	0.0104	0.0083	0.0049	0.0019	**0.0015**
	30 dB	5%	MPSNR	13.557	14.291	20.835	28.402	29.586	24.838	**32.150**
			MSSIM	0.0253	0.0860	0.3169	0.8387	0.8706	0.7875	**0.9138**
			MSAM	77.288	52.198	9.7647	11.593	**7.3525**	13.838	9.0924
			NMSE	0.9502	0.8081	0.1753	0.0358	0.0234	0.0912	**0.0177**
		15%	MPSNR	14.040	24.303	26.135	34.814	41.131	37.311	**42.172**
			MSSIM	0.0694	0.6502	0.7291	0.9436	0.9865	0.9763	**0.9893**
			MSAM	67.422	10.235	7.7719	7.9426	4.0853	4.5661	**3.4985**
			NMSE	0.8502	0.0787	0.0509	0.0098	0.0015	0.0042	**0.0015**
		25%	MPSNR	14.583	27.996	29.790	38.042	43.938	42.873	**45.897**
			MSSIM	0.1184	0.8311	0.8813	0.9678	0.9926	0.9937	**0.9955**
			MSAM	60.222	8.6521	6.4283	6.3472	3.1420	2.6773	**2.3635**
			NMSE	0.7508	0.0334	0.0215	0.0050	0.0008	0.0012	**0.0006**
		50%	MPSNR	16.343	34.841	35.692	41.035	45.087	45.462	**48.573**
			MSSIM	0.2601	0.9601	0.9674	0.9829	0.9943	0.9965	**0.9962**
			MSAM	45.385	6.0001	4.8786	4.8723	2.8613	**2.1584**	2.2669
			NMSE	0.5013	0.0068	0.0054	0.0022	0.0006	0.0006	**0.0005**

HSI data: All our experiments are performed on two HSI datasets, namely Washington DC (WDC) with the size of $256 \times 256 \times 191$ and Pavia University (PaU) with the size of $200 \times 200 \times 80$. These HSIs are used as benchmark test datasets for HSI reconstruction problems [56]–[60]. In the experiment, we add Gaussian independent and uniformly distributed noise with signal-to-noise ratio (SNR) {20 dB, 30 dB} under different sampling rates {5%, 15%, 25%, 50%}.

Parameter Setting: It is very important to set appropriate parameters for each algorithm. In this article, the model parameters of the proposed algorithm are λ_1, λ_2, and p, the proximal parameter is ρ, and the maximum number of outer iterations

TABLE IV
AVERAGE COMPUTATIONAL TIMES (IN SECONDS) OF COMPARED METHODS ON TWO DATASETS

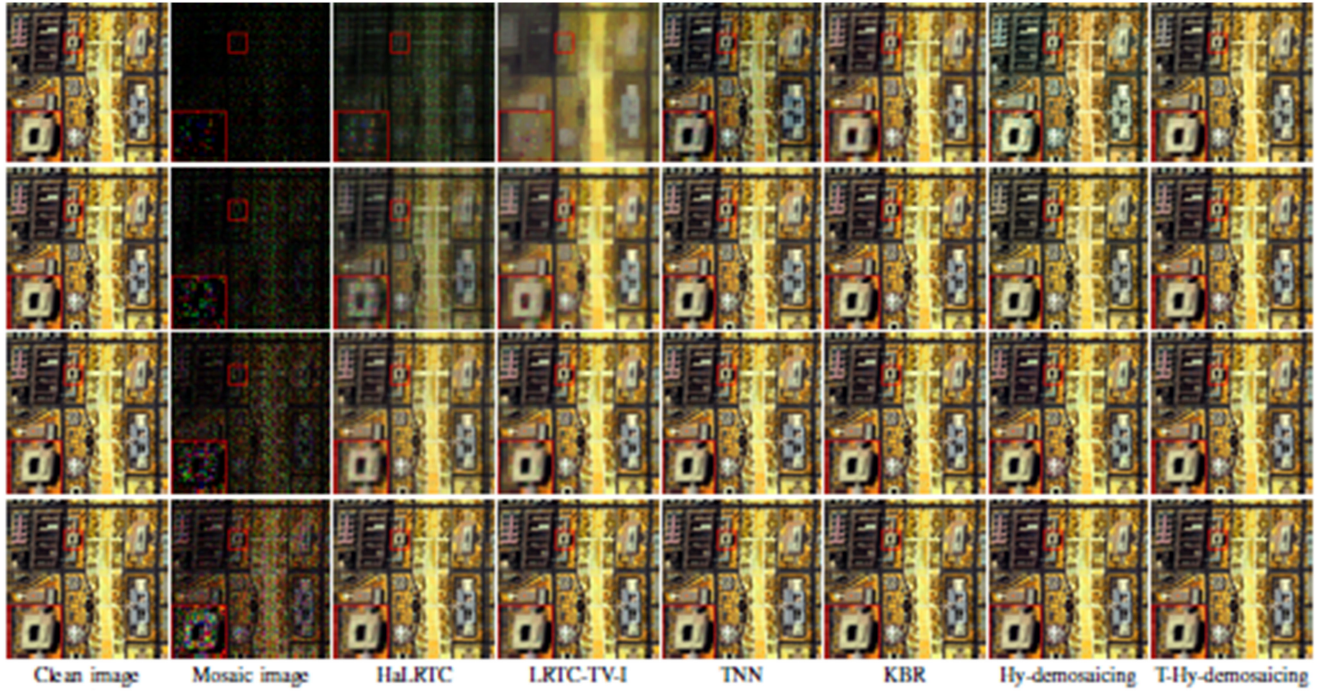| Methods / Dataset	HaLRTC	LRTC-TV-I	TNN	KBR	Hy-demosaicing	T-Hy-demosaicing
WDC	96.301	2173.8	470.43	1868.1	170.04	584.06
PaU	22.824	426.16	87.908	503.43	89.041	240.13

Fig. 5. Visual reconstructed results on pseudo-color images (R: 70 G: 100 B: 160) of the Washington DC from the compared methods under noise SNR = 30 dB. Top to bottom row represents the sampling rate of 5%, 15%, 25%, and 50%.
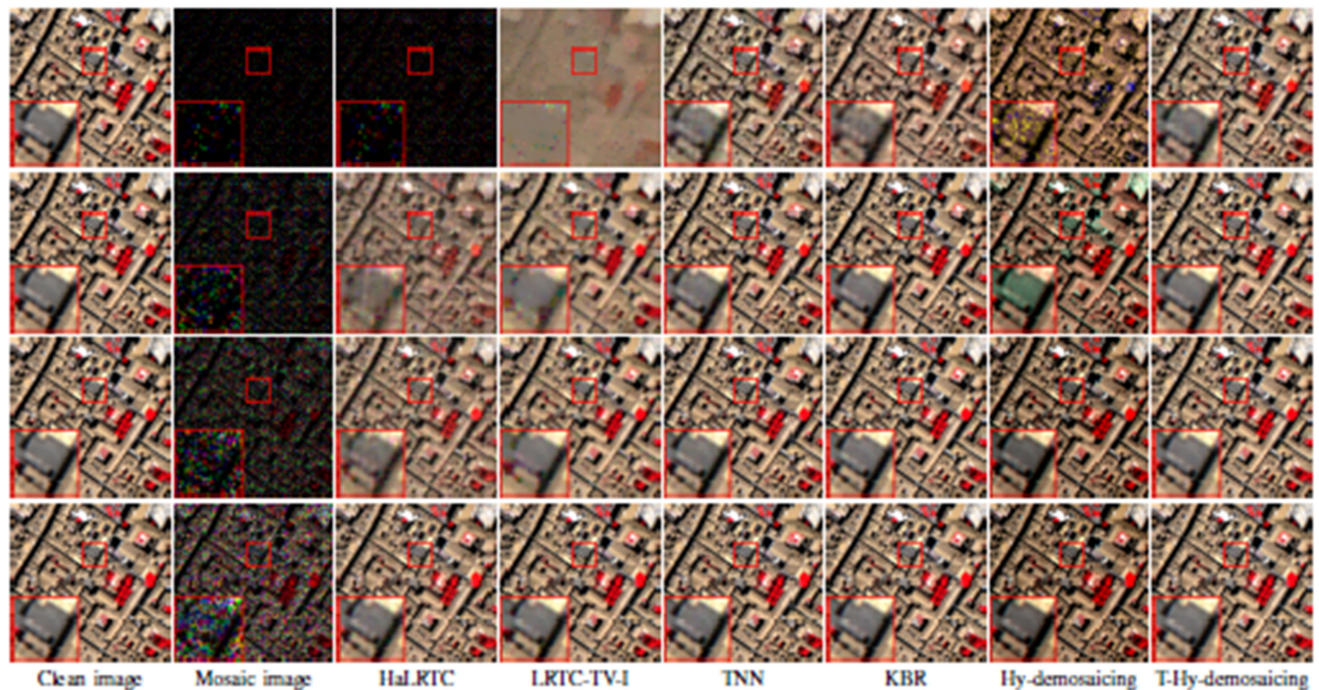
Fig. 6. Visual reconstructed results on pseudo-color images (R: 60 G: 40 B: 20) of the Pavia University from the compared methods under noise SNR = 30 dB. Top to bottom row represents the sampling rate of 5%, 15%, 25%, and 50%.

is M. The spectral dimension p is highly correlated with the number of spectrum samples and noise level, and its value is shown in Table I. The regularization parameters λ_1 and λ_2 need to be adjusted based on experience, and the tuning range is $\{10^{-4}, 10^{-3}, 10^{-2}, 10^{-1}, 1, 10\}$. The algorithm parameters are set to $\rho = 10^{-5}$, $M = 50$. We adjust the parameter settings of the compared methods according to the author's paper or code suggestions to get the best results. The critical parameters of compared methods are in Table II.

Reconstruction Quality Indices: We use the mean of peak-signal-to-noise ratio (MPSNR), mean of structural similarity index measure (MSSIM), spectral angle mapper (MSAM), and normalized mean squared error (NMSE) to measure the quality of the reconstruction results. Let $\mathcal{X} \in \mathbb{R}^{m \times n \times b}$ and $\mathcal{X}_r \in \mathbb{R}^{m \times n \times b}$ represent the original clean HSI and reconstructed HSI, respectively. These four indices are defined as follows:

$$\text{MPSNR}(\mathcal{X}_r, \mathcal{X}) = \frac{1}{b} \sum_{k=1}^{b} 10\log_{10} \left(\frac{255^2 mn}{\|\mathcal{X}_r(:,:,k) - \mathcal{X}(:,:,k)\|_F^2} \right)$$

$$\text{MSSIM}(\mathcal{X}_r, \mathcal{X}) = \frac{1}{b} \sum_{k=1}^{b} \text{SSIM}(\mathcal{X}_r(:,:,k), \mathcal{X}(:,:,k))$$

$$\text{NMSE}(\mathcal{X}_r, \mathcal{X}) = \frac{\|\mathcal{X} - \mathcal{X}_r\|_F^2}{\|\mathcal{X}\|_F^2}$$

$$\text{MSAM}(\mathcal{X}_r, \mathcal{X}) = \frac{1}{mn} \sum_{i=1}^{m} \sum_{j=1}^{n} \cos^{-1} \frac{\mathbf{x}^T \mathbf{x}_r}{(\mathbf{x}^T \mathbf{x})^{1/2} (\mathbf{x}_r^T \mathbf{x}_r)^{1/2}}$$

where the definition of $\text{SSIM}(\mathcal{X}_r(:,:,k), \mathcal{X}(:,:,k))$ can be seen in [61] and $\mathbf{x} = \text{vec}(\mathcal{X}(i,j,:))$, $\mathbf{x}_r = \text{vec}(\mathcal{X}_r(i,j,:))$. Generally, high-quality reconstructed HSI has larger MPSNR and MSSIM values, and smaller NMSE and MSAM values.

A. Quantitative Comparision

Table III lists the quantitative performance of different methods in simulating HSI demosaicing. It can be observed that compared with other methods, our method always produces best performance in terms of MPSNR, MSSIM, MSAM, and NMSE in most cases (in the case of low sampling, while the index gap with the first best method is very small). Specifically, compared with the classic demosaicing method Hy-demosaicing, the proposed method achieves a competitive performance. This verifies the advantages of our self-updated tensor subspace compared to the traditional matrix subspace. Compared with KBR, our method can also improve 0.6 dB or more in most cases. Moreover, compared with the traditional completion methods, our method can handle a certain range of Gaussian noise, which enhances the robustness of the algorithm. In addition, we report the average computational times (in seconds) of compared methods on both WDC and PaU datasets as shown in Table IV. We can observe that the Hy-demosaicing method is faster and KBR is slower with the guarantee of getting a good reconstruction. Overall, the proposed method achieves the efficiency tradeoff.
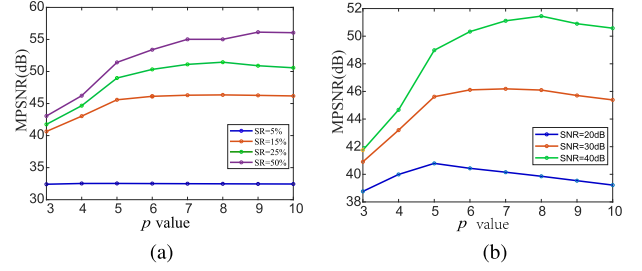

Fig. 7. MPSNR values achieved by the proposed method with different parameter p with SNR = 40 dB or sampling rate 25% on the WDC dataset.
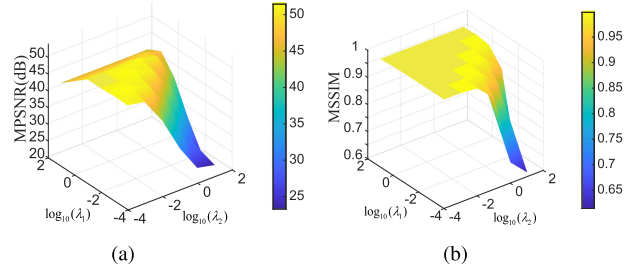

Fig. 8. MPSNR and MSSIM values of the results with respect to λ_1 and λ_2 on the WDC dataset for the sampling rate 25%, respectively.
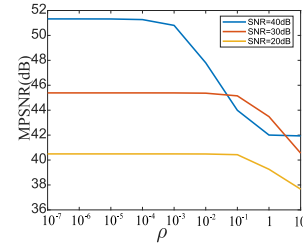

Fig. 9. MPSNR values with respect to ρ at sampling rate 25% on the WDC dataset.

B. Visual Comparison

Figs. 5 and 6 show the visual results obtained by adding noise level SNR = 30 dB to the above two datasets under different sampling rates. Including five compared methods, we also give the original clean image as a reference. We can see that the mosaic images retain limited image information, especially in cases below 15% sampling rate. For the low sampling rate cases, the demosaicing results from compared methods show that HaLRTC and LRTC-TV-I cannot cope with such severe degradation; TNN leaves some relatively obvious noise in the whole image; Hy-demosaicing can eliminate more noise, but overprocessing will lose tiny image details and its reconstructed images have subtle color distortion visual perception as a whole. It is worth noting that the KBR method and our proposed T-Hy-demosaicing method have obtained relatively good visual effects on several experimental datasets. In fact, the visual compared results are not very obvious in the display of the more detailed parts. However, in view of the above reconstruction quality indices, our proposed algorithm still has a relatively superior performance.
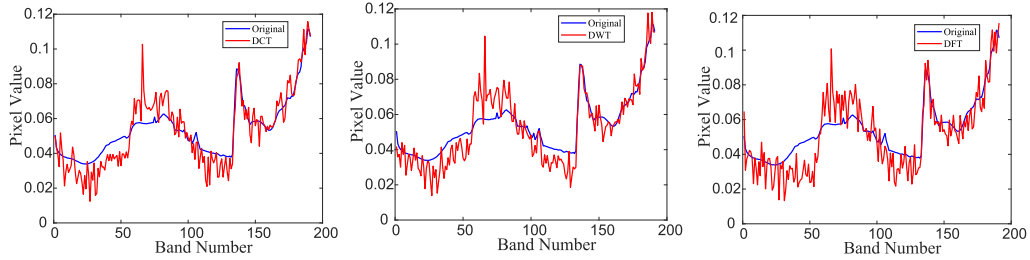
Fig. 10. Spectrum profiles of pixels (256,25) on the WDC dataset with SNR = 20 dB and sampling rate 25% obtained by DCT, DWT, and DFT.

C. Discussions

1) Parameter Analysis: The proposed T-Hy-demosaicing method involves three important parameters: the subspace dimension p, and the regularization parameters λ_1 and λ_2, and the proximal parameter ρ. In the following, we will discuss the sensitivity analysis of these parameters.

a) The subspace dimension p mainly characterizes the spatial and spectral information of HSI. The sensitivity analysis of p is shown in Fig. 7. It can be seen that the setting of the subspace dimension p-value has a higher correlation with the sampling rate and noise level. Generally, the higher the sampling rate, the lower the noise level, the larger the p-value. However, the proposed algorithm shows stable and superior performance in the specific range of p. Considering that a larger p will lead to higher computational complexity, we set the value of p according to the number of sampled spectra and the noise level, as shown in Table I.

b) The parameters λ_1 and λ_2, respectively, determine the weights of the tensor subspace decomposition term and the nonlocal low-tubal-rank regularization term. In addition, they are also used to estimate the noise level in the WNNM denoiser. Fig. 8 shows their sensitivity analysis of T-Hy-demosaicing on the WDC, with a fixed sampling rate of 25% and a noise level of SNR = 40 dB. As observed, when the values of λ_1 and λ_2 are as consistent as possible, the experimental results obtained are better, and the best reconstruction effect is achieved when $\lambda_1 = 10^{-2}$ and $\lambda_2 = 10^{-2}$.

c) The proximal parameter ρ is the primal parameter that guarantees the convergence of the PAM algorithm. We select the ρ from the candidate set $\{10^{-7}, 10^{-6}, 10^{-5}, 10^{-4}, 10^{-3}, 10^{-2}, 10^{-1}, 1, 10\}$. Fig. 9 shows the MPSNR of the proposed method for different noise levels at sampling rate 25% on the WDC dataset. We can observe that the MPSNR is maintained at a high value under different noise levels when ρ is smaller than 10^{-3}. Considering the effect and the convergence, we set $\rho = 10^{-5}$ in our method.

2) Influence of Transformation: We analyze the effect of the reconstruction results from using tensor decomposition based on different orthogonal transformations on the demosaicing problem. Fig. 10 plots the spectrum profiles of pixels (256,25) on the WDC dataset with SNR = 20 dB and sampling rate 25% obtained by DCT, DFT, and discrete wavelet transform (DWT).
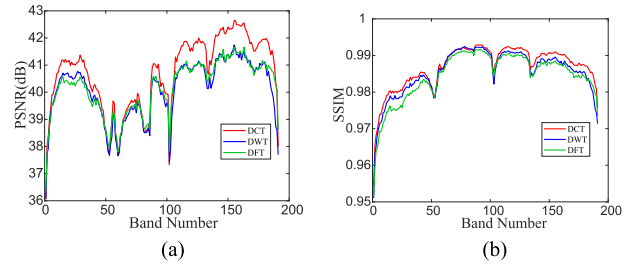

(a)   (b)

Fig. 11. PSNR and SSIM values of each band of the recovered HSI WDC dataset with SNR = 20 dB and sampling rate 25% obtained by DCT, DWT, and DFT.
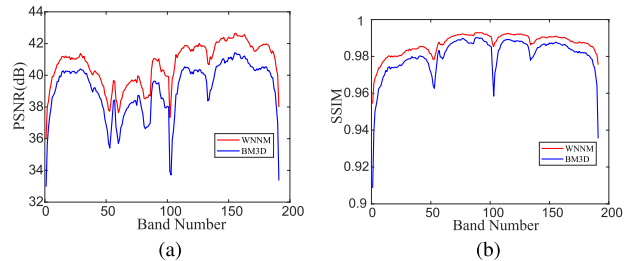

(a)   (b)

Fig. 12. PSNR and SSIM values of each band of the recovered HSI WDC dataset with SNR = 20 dB and sampling rate 25% obtained by WNNM and BM3D.

Among them, DCT deviates less from the original curve in some frequency bands and can retain more spectrum information, especially at the boundary. In addition, Fig. 11 shows the PSNR value and SSIM value of each band of the HSI recovered through the DCT, DFT, and DWT. We can observe that the results of DCT are higher than those of DFT and DWT, which also indicates to some extent that the representation capability of the subspace learned based on DCT is better than that based on DFT and DWT. In summary, DCT is a relatively better choice for the demosaicing problem that belongs to the category of compression problems, and can retain more information of the HSI.

3) Influence of Denoiser: We analyze the reconstruction effect of using various denoisers for solving the $\mathcal{Z}$ subproblem in the Hy-demosaicing method. Fig. 12 presents the PSNR value and SSIM value of each band obtained by using WNNM and BM3D, respectively, on the WDC dataset with SNR = 20 dB and sampling rate 25%. It can be seen that, compared with the BM3D
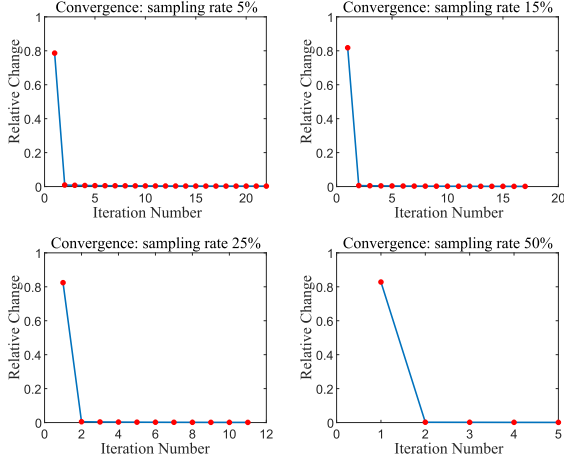
Fig. 13. Convergence behavior of the PAM algorithm under different sampling rates on the WDC dataset.

method, the WNNM method can obtain a better reconstruction effect. Therefore, the entire experimental part of our article uses the WNNM denoiser to solve the $\mathcal{Z}$ subproblem in the algorithm.

4) Convergence Behavior: We analyze the convergence of the proposed PAM algorithm. In Fig 13, we use the T-Hy-demosaicing algorithm to process the HSI WDC, showing the relative change curve with respect to the number of iterations, and the sampling rates are 5%, 15%, 25%, and 50%, respectively. It can be observed that for different sampling rates, as the number of iterations increases, the relative change value obtained at each step of the algorithm decreases monotonically and gradually tends to zero. This verifies the strong numerical convergence of the proposed PAM-based T-Hy-demosaicing algorithm.

V. CONCLUSION

In this article, we propose a hyperspectral demosaicing method based on a new hyperspectral sensing framework, which exploits both low-tubal-rankness and nonlocal self-similarity. Based on the low-tubal-rankness, the HSI can be naturally represented by the subspace basis and coefficient tensor. For learning subspace basis, we suggest a novel t-SVD based on orthogonal transformation. Under the decomposition, we flexibly choose appropriate transformation to learn subspaces, and the learned subspace has better representation ability. Moreover, through the subspace representation, the original high-dimensional problem is converted to deal with the low-dimensional coefficient tensor, and its inherited nonlocal self-similarity can be exploited by the PnP denoiser, which greatly reduces the computational complexity. Numerical experiments show the superiority of the proposed T-Hy-demosaicing method.

APPENDIX

Theorem 1: Let $\mathbf{A}$ be a semiorthogonal matrix, i.e. $\mathbf{A}^{\mathsf{T}}\mathbf{A} = \mathbf{I}$, where $\mathbf{I}$ is the identity matrix. Then, we have

$$\arg\min_{\mathbf{Z}} \|\mathbf{X} - \mathbf{A}\mathbf{Z}\|_F^2 = \arg\min_{\mathbf{Z}} \|\mathbf{A}^{\mathsf{T}}\mathbf{X} - \mathbf{Z}\|_F^2.$$

Proof: From $\mathbf{A}$ is a semiorthogonal matrix, it follows that

$$\|\mathbf{A}\mathbf{X}\|_F^2 = \operatorname{trace}\left((\mathbf{A}\mathbf{X})^{\mathsf{T}}\mathbf{A}\mathbf{X}\right) = \operatorname{trace}\left(\mathbf{X}^{\mathsf{T}}\mathbf{A}^{\mathsf{T}}\mathbf{A}\mathbf{X}\right)$$
$$= \operatorname{trace}(\mathbf{X}^{\mathsf{T}}\mathbf{X}) = \|\mathbf{X}\|_F^2. \tag{13}$$

Moreover, we have the following equation:

$$\mathbf{Z} = \arg\min_{\mathbf{Z}} \|\mathbf{X} - \mathbf{A}\mathbf{Z}\|_F^2$$
$$= \arg\min_{\mathbf{Z}} \left\|\mathbf{A}\mathbf{A}^{\mathsf{T}}\mathbf{X} - \mathbf{A}\mathbf{Z} - \left(\mathbf{A}\mathbf{A}^{\mathsf{T}} - \mathbf{I}\right)\mathbf{X}\right\|_F^2. \tag{14}$$

Set $\mathbf{B}_1 = \mathbf{A}\mathbf{A}^{\mathsf{T}}\mathbf{X} - \mathbf{A}\mathbf{Z}$, $\mathbf{B}_2 = (\mathbf{A}\mathbf{A}^{\mathsf{T}} - \mathbf{I})\mathbf{X}$. From (14), we obtain

$$\|\mathbf{B}_1 - \mathbf{B}_2\|_F^2 = \operatorname{trace}\left((\mathbf{B}_1 - \mathbf{B_2})^{\mathsf{T}}(\mathbf{B}_1 - \mathbf{B_2})\right)$$
$$= \operatorname{trace}\left(\mathbf{B}_1^{\mathsf{T}}\mathbf{B}_1 + \mathbf{B}_2^{\mathsf{T}}\mathbf{B}_2 - \mathbf{B}_1^{\mathsf{T}}\mathbf{B}_2 - \mathbf{B}_2^{\mathsf{T}}\mathbf{B}_1\right)$$

and

$$\operatorname{trace}(\mathbf{B}_1^{\mathsf{T}}\mathbf{B}_2) = \operatorname{trace}\left(\left(\mathbf{A}\mathbf{A}^{\mathsf{T}}\mathbf{X} - \mathbf{A}\mathbf{Z}\right)^{\mathsf{T}}\left(\mathbf{A}\mathbf{A}^{\mathsf{T}} - \mathbf{I}\right)\mathbf{X}\right)$$
$$= \operatorname{trace}\left(\mathbf{X}^{\mathsf{T}}\mathbf{A}\mathbf{A}^{\mathsf{T}}\left(\mathbf{A}\mathbf{A}^{\mathsf{T}} - \mathbf{I}\right)\mathbf{X} - \mathbf{Z}^{\mathsf{T}}\mathbf{A}^{\mathsf{T}}\left(\mathbf{A}\mathbf{A}^{\mathsf{T}} - \mathbf{I}\right)\mathbf{X}\right)$$
$$= \operatorname{trace}\left(\mathbf{X}^{\mathsf{T}}\mathbf{A}\mathbf{A}^{\mathsf{T}}\mathbf{X} - \mathbf{X}^{\mathsf{T}}\mathbf{A}\mathbf{A}^{\mathsf{T}}\mathbf{X} - \mathbf{Z}^{\mathsf{T}}\mathbf{A}^{\mathsf{T}}\mathbf{X} + \mathbf{Z}^{\mathsf{T}}\mathbf{A}^{\mathsf{T}}\mathbf{X}\right)$$
$$= 0.$$

Since $\operatorname{trace}(\mathbf{B}_1^{\mathsf{T}}\mathbf{B}_2) = \operatorname{trace}(\mathbf{B}_2^{\mathsf{T}}\mathbf{B}_1) = 0$, we have

$$\|\mathbf{B}_1 - \mathbf{B}_2\|_F^2 = \operatorname{trace}(\mathbf{B}_1^{\mathsf{T}}\mathbf{B}_1 + \mathbf{B}_2^{\mathsf{T}}\mathbf{B}_2) = \|\mathbf{B}_1\|_F^2 + \|\mathbf{B}_2\|_F^2$$

which combining with the definition of $\mathbf{B}_1$ and (13) yields that

$$\arg\min_{\mathbf{B}_1} \|\mathbf{B}_1 - \mathbf{B}_2\|_F^2 = \arg\min_{\mathbf{B}_1} \|\mathbf{B}_1\|_F^2$$
$$= \arg\min_{\mathbf{Z}} \left\|\mathbf{A}\mathbf{A}^{\mathsf{T}}\mathbf{X} - \mathbf{A}\mathbf{Z}\right\|_F^2$$
$$= \arg\min_{\mathbf{Z}} \left\|\mathbf{A}^{\mathsf{T}}\mathbf{X} - \mathbf{Z}\right\|_F^2.$$

The proof is completed. ∎

REFERENCES

[1] J. Jia, Y. Wang, J. Chen, R. Guo, R. Shu, and J. Wang, "Status and application of advanced airborne hyperspectral imaging technology: A review," *Infrared Phys. Technol.*, vol. 104, 2020, Art. no. 103115.

[2] Y. Lu, W. Saeys, M. Kim, Y. Peng, and R. Lu, "Hyperspectral imaging technology for quality and safety evaluation of horticultural products: A review and celebration of the past 20-year progress," *Postharvest Biol. Technol.*, vol. 170, 2020, Art. no. 111318.

[3] W. He, H. Zhang, and L. Zhang, "Sparsity-regularized robust non-negative matrix factorization for hyperspectral unmixing," *IEEE J. Sel. Topics Appl. Earth Observ. Remote Sens.*, vol. 9, no. 9, pp. 4267–4279, Sep. 2016.

[4] Y. Chang, L. Yan, H. Fang, S. Zhong, and W. Liao, "HSI-DeNet: Hyperspectral image restoration via convolutional neural network," *IEEE Trans. Geosci. Remote Sens.*, vol. 57, no. 2, pp. 667–682, Feb. 2019.

[5] X.-L. Zhao, W.-H. Xu, T.-X. Jiang, Y. Wang, and M. K. Ng, "Deep plug-and-play prior for low-rank tensor completion," *Neurocomputing*, vol. 400, pp. 137–149, 2020.

[6] Y.-Y. Liu, X.-L. Zhao, Y.-B. Zheng, T.-H. Ma, and H. Zhang, "Hyperspectral image restoration by tensor fibered rank constrained optimization and plug-and-play regularization," *IEEE Trans. Geosci. Remote Sens.*, to be published, doi: 10.1109/TGRS.2020.3045169.

[7] L. Zhuang, X. Fu, M. K. Ng, and J. M. Bioucas-Dias, "Hyperspectral image denoising based on global and nonlocal low-rank factorizations," *IEEE Trans. Geosci. Remote Sens.*, to be published, doi: 10.1109/TGRS.2020.3046038.

[8] T.-X. Jiang, M. K. Ng, X.-L. Zhao, and T.-Z. Huang, "Framelet representation of tensor nuclear norm for third-order tensor completion," *IEEE Trans. Image Process.*, vol. 29, pp. 7233–7244, 2020.

[9] A. Sumarsono and Q. Du, "Low-rank subspace representation for supervised and unsupervised classification of hyperspectral imagery," *IEEE J. Sel. Topics Appl. Earth Observ. Remote Sens.*, vol. 9, no. 9, pp. 4188–4195, Sep. 2016.

[10] L. He, J. Zhu, J. Li, D. Meng, J. Chanussot, and A. Plaza, "Spectral-fidelity convolutional neural networks for hyperspectral pansharpening," *IEEE J. Sel. Topics Appl. Earth Observ. Remote Sens.*, vol. 13, pp. 5898–5914, 2020.

[11] S. Li and B. Yang, "A new pan-sharpening method using a compressed sensing technique," *IEEE Trans. Geosci. Remote Sens.*, vol. 49, no. 2, pp. 738–746, Feb. 2011.

[12] L. Zhang, W. Wei, C. Tian, F. Li, and Y. Zhang, "Exploring structured sparsity by a reweighted laplace prior for hyperspectral compressive sensing," *IEEE Trans. Image Process.*, vol. 25, no. 10, pp. 4974–4988, Oct. 2016.

[13] J. Xue, Y. Zhao, W. Liao, and J. C.-W. Chan, "Nonlocal tensor sparse representation and low-rank regularization for hyperspectral image compressive sensing reconstruction," *Remote Sens.*, vol. 11, no. 2, 2019, Art. no. 193.

[14] L. Wang, Y. Feng, Y. Gao, Z. Wang, and M. He, "Compressed sensing reconstruction of hyperspectral images based on spectral unmixing," *IEEE J. Sel. Topics Appl. Earth Observ. Remote Sens.*, vol. 11, no. 4, pp. 1266–1284, Apr. 2018.

[15] J. Xue, Y. Zhao, W. Liao, and J. C.-W. Chan, "Hyper-laplacian regularized nonlocal low-rank matrix recovery for hyperspectral image compressive sensing reconstruction," *Inf. Sci.*, vol. 501, pp. 406–420, 2019.

[16] J. Yang, Y. Zhang, and W. Yin, "A fast alternating direction method for TVl_1 $-$ l_2 signal reconstruction from partial fourier data," *IEEE J. Sel. Topics Signal Process.*, vol. 4, no. 2, pp. 288–297, Apr. 2010.

[17] R. Zhao, Q. Wang, J. Fu, and L. Ren, "Exploiting block-sparsity for hyperspectral kronecker compressive sensing: A tensor-based bayesian method," *IEEE Trans. Image Process.*, vol. 29, pp. 1654–1668, 2019.

[18] G. Martín and J. M. Bioucas-Dias, "Hyperspectral compressive acquisition in the spatial domain via blind factorization," in *Proc. 7th Workshop Hyperspectral Image Signal Process., Evol. Remote Sens.*, 2015, pp. 1–4.

[19] R. Zhao, Q. Wang, and Y. Shen, "Kronecker compressive sensing-based mechanism with fully independent sampling dimensions for hyperspectral imaging," *J. Electron. Imag.*, vol. 24, no. 6, 2015, Art. no. 063012.

[20] Y. August, C. Vachman, Y. Rivenson, and A. Stern, "Compressive hyperspectral imaging by random separable projections in both the spatial and the spectral domains," *Appl. Opt.*, vol. 52, no. 10, pp. D46–D54, 2013.

[21] L. Zhang, L. Zhang, D. Tao, X. Huang, and B. Du, "Compression of hyperspectral remote sensing images by tensor approach," *Neurocomputing*, vol. 147, pp. 358–363, 2015.

[22] X. Zhang and X. Zhang, "Compressive hyperspectral imaging with spatial and spectral priors," *IEEE J. Sel. Topics Appl. Earth Observ. Remote Sens.*, vol. 11, no. 11, pp. 4156–4169, Nov. 2018.

[23] L. Zhang *et al.*, "Cluster sparsity field: An internal hyperspectral imagery prior for reconstruction," *Int. J. Comput. Vis.*, vol. 126, no. 8, pp. 797–821, 2018.

[24] Y. Liu, X. Yuan, J. Suo, D. J. Brady, and Q. Dai, "Rank minimization for snapshot compressive imaging," *IEEE Trans. Pattern Anal. Mach. Intell.*, vol. 41, no. 12, pp. 2990–3006, Dec. 2019.

[25] T. Xie, S. Li, and B. Sun, "Hyperspectral compressive sensing via spatial-spectral total variation regularized low-rank tensor decomposition," in *Proc. Int. Geosci. Remote Sens. Symp.*, 2019, pp. 1963–1966.

[26] Y. Chen, T. Huang, W. He, N. Yokoya, and X. Zhao, "Hyperspectral image compressive sensing reconstruction using subspace-based nonlocal tensor ring decomposition," *IEEE Trans. Image Process.*, vol. 29, pp. 6813–6828, 2020.

[27] D. L. Donoho, "Compressed sensing," *IEEE Trans. Inf. Theory*, vol. 52, no. 4, pp. 1289–1306, Apr. 2006.

[28] L. Zhuang and J. M. Bioucas-Dias, "Hy-Demosaicing: Hyperspectral Blind Reconstruction From Spectral Subsampling," in *Proc. Int. Geosci. Remote Sens. Symp.*, 2018, pp. 4015–4018.

[29] Y. Chang, L. Yan, X.-L. Zhao, H. Fang, Z. Zhang, and S. Zhong, "Weighted low-rank tensor recovery for hyperspectral image restoration," *IEEE Trans. Cybern.*, vol. 50, no. 11, pp. 4558–4572, Nov. 2020.

[30] W. He, H. Zhang, H. Shen, and L. Zhang, "Hyperspectral image denoising using local low-rank matrix recovery and global spatial-spectral total variation," *IEEE J. Sel. Topics Appl. Earth Observ. Remote Sens.*, vol. 11, no. 3, pp. 713–729, Mar. 2018.

[31] L. Zhuang and J. M. Bioucas-Dias, "Fast hyperspectral image denoising and inpainting based on low-rank and sparse representations," *IEEE J. Sel. Top. Appl. Earth Observ. Remote Sens.*, vol. 11, no. 3, pp. 730–742, Mar. 2018.

[32] P. Zheng, H. Su, and Q. Du, "Sparse and low-rank constrained tensor factorization for hyperspectral image unmixing," *IEEE J. Sel. Topics Appl. Earth Observ. Remote Sens.*, vol. 14, pp. 1754–1767, 2021.

[33] X. Xu, J. Li, S. Li, and A. Plaza, "Curvelet transform domain-based sparse nonnegative matrix factorization for hyperspectral unmixing," *IEEE J. Sel. Topics Appl. Earth Observ. Remote Sens.*, vol. 13, pp. 4908–4924, 2020.

[34] J.-L. Wang, T.-Z. Huang, X.-L. Zhao, J. Huang, T.-H. Ma, and Y.-B. Zheng, "Reweighted block sparsity regularization for remote sensing images destriping," *IEEE J. Sel. Topics Appl. Earth Observ. Remote Sens.*, vol. 12, no. 12, pp. 4951–4963, Dec. 2019.

[35] M. E. Kilmer and C. D. Martin, "Factorization strategies for third-order tensors," *Linear Algebra its Appl.*, vol. 435, no. 3, pp. 641–658, 2011.

[36] G. Song, M. K. Ng, and X. Zhang, "Robust tensor completion using transformed tensor singular value decomposition," *Numer. Linear Algebra Appl.*, vol. 27, no. 3, 2020, Art. no. e2299.

[37] W.-H. Xu, X.-L. Zhao, and M. Ng, "A fast algorithm for cosine transform based tensor singular value decomposition," 2019, *arXiv:1902.03070*.

[38] H. Zhang, W. He, L. Zhang, H. Shen, and Q. Yuan, "Hyperspectral image restoration using low-rank matrix recovery," *IEEE Trans. Geosci. Remote Sens.*, vol. 52, no. 8, pp. 4729–4743, Aug. 2014.

[39] Y. Chen, W. He, N. Yokoya, and T.-Z. Huang, "Hyperspectral image restoration using weighted group sparsity-regularized low-rank tensor decomposition," *IEEE Trans. Cybern.*, vol. 50, no. 8, pp. 3556–3570, Aug. 2020.

[40] M. Ding, T.-Z. Huang, X.-L. Zhao, M. K. Ng, and T.-H. Ma, "Tensor train rank minimization with nonlocal self-similarity for tensor completion," *Inverse Problems Imag.*, 2021, doi: 10.3934/IPI.2021001.

[41] X. Zhang and M. K.-P. Ng, "Low rank tensor completion with poisson observations," *IEEE Trans. Pattern Anal. Mach. Intell.*, 2021, doi: 10.1109/TPAMI.2021.3059299.

[42] W. He, Q. Yao, C. Li, N. Yokoya, and Q. Zhao, "Non-local meets global: An integrated paradigm for hyperspectral denoising," in *Proc. IEEE/CVF Conf. Comput. Vis. Pattern Recognit.*, 2019, pp. 6861–6870.

[43] X.-L. Lin, M. K. Ng, and X.-L. Zhao, "Tensor factorization with total variation and Tikhonov regularization for low-rank tensor completion in imaging data," *J. Math. Imag. Vis.*, vol. 62, no. 6, pp. 900–918, 2020.

[44] J.-L. Wang, T.-Z. Huang, X.-L. Zhao, T.-X. Jiang, and M. K. Ng, "Multi-dimensional visual data completion via low-rank tensor representation under coupled transform," *IEEE Trans. Image Process.*, to be published, doi: 10.1109/TIP.2021.3062995.

[45] H. Attouch, J. Bolte, P. Redont, and A. Soubeyran, "Proximal alternating minimization and projection methods for nonconvex problems: An approach based on the kurdyka-łojasiewicz inequality," *Math. Operations Res.*, vol. 35, no. 2, pp. 438–457, 2010.

[46] H. Attouch, J. Bolte, and B. F. Svaiter, "Convergence of descent methods for semi-algebraic and tame problems: Proximal algorithms, forward-backward splitting, and regularized Gauss-Seidel methods," *Math. Program.*, vol. 137, no. 1–2, pp. 91–129, 2013.

[47] N. Yair and T. Michaeli, "Multi-scale weighted nuclear norm image restoration," in *Proc. IEEE Conf. Comput. Vis. Pattern Recognit.*, 2018, pp. 3165–3174.

[48] S. Gu, L. Zhang, W. Zuo, and X. Feng, "Weighted nuclear norm minimization with application to image denoising," in *Proc. IEEE Conf. Comput. Vis. Pattern Recognit.*, 2014, pp. 2862–2869.

[49] J. Xu, L. Zhang, D. Zhang, and X. Feng, "Multi-channel weighted nuclear norm minimization for real color image denoising," in *Proc. Int. Conf. Comput. Vis.*, 2017, pp. 1096–1104.

[50] K. Dabov, A. Foi, V. Katkovnik, and K. Egiazarian, "Image denoising by sparse 3-d transform-domain collaborative filtering," *IEEE Trans. Image Process.*, vol. 16, no. 8, pp. 2080–2095, Aug. 2007.

[51] J. Lin, T. Z. Huang, X. L. Zhao, T. X. Jiang, and L. Zhuang, "A tensor subspace representation-based method for hyperspectral image denoising," *IEEE Trans. Geosci. Remote Sens.*, to be published, doi: 10.1109/TGRS.2020.3032168.

[52] J. Liu, P. Musialski, P. Wonka, and J. Ye, "Tensor completion for estimating missing values in visual data," *IEEE Trans. Pattern Anal. Mach. Intell.*, vol. 35, no. 1, pp. 208–220, Jan. 2013.

[53] X. Li, Y. Ye, and X. Xu, "Low-rank tensor completion with total variation for visual data inpainting," in *Proc. 31st AAAI Conf. Artif. Intell.*, 2017, pp. 2210–2216.

[54] Z. Zhang, G. Ely, S. Aeron, N. Hao, and M. Kilmer, "Novel methods for multilinear data completion and de-noising based on tensor-SVD," in *Proc. IEEE Conf. Comput. Vis. Pattern Recognit.*, 2014, pp. 3842–3849.

[55] Q. Xie, Q. Zhao, D. Meng, and Z. Xu, "Kronecker-basis-representation based tensor sparsity and its applications to tensor recovery," *IEEE Trans. Pattern Anal. Mach. Intell.*, vol. 40, no. 8, pp. 1888–1902, Aug. 2018.

[56] Y. Chen, W. He, N. Yokoya, T. Huang, and X. Zhao, "Nonlocal tensor-ring decomposition for hyperspectral image denoising," *IEEE Trans. Geosci. Remote Sens.*, vol. 58, no. 2, pp. 1348–1362, Feb. 2020.

[57] L. Zhuang, L. Gao, B. Zhang, X. Fu, and J. M. Bioucas-Dias, "Hyperspectral image denoising and anomaly detection based on low-rank and sparse representations," *IEEE Trans. Geosci. Remote Sens.*, to be published, doi: 10.1109/TGRS.2020.3040221.

[58] J.-H. Yang, X.-L. Zhao, T.-H. Ma, Y. Chen, T.-Z. Huang, and M. Ding, "Remote sensing images destriping using unidirectional hybrid total variation and nonconvex low-rank regularization," *J. Comput. Appl. Math.*, vol. 363, pp. 124–144, 2020.

[59] Y.-B. Zheng, T.-Z. Huang, X.-L. Zhao, T.-X. Jiang, T.-H. Ma, and T.-Y. Ji, "Mixed noise removal in hyperspectral image via low-fibered-rank regularization," *IEEE Trans. Geosci. Remote Sens.*, vol. 58, no. 1, pp. 734–749, Jan. 2020.

[60] Y.-B. Zheng, T.-Z. Huang, X.-L. Zhao, Y. Chen, and W. He, "Double-factor-regularized low-rank tensor factorization for mixed noise removal in hyperspectral image," *IEEE Trans. Geosci. Remote Sens.*, vol. 58, no. 12, pp. 8450–8464, Dec. 2020.

[61] Z. Wang, A. C. Bovik, H. R. Sheikh, and E. P. Simoncelli, "Image quality assessment: From error visibility to structural similarity," *IEEE Trans. Image Process.*, vol. 13, no. 4, pp. 600–612, Apr. 2004.

Jie Lin received the B.S. degree in information and computing science from Anhui University of Finance and Economics, Bengbu, China, in 2018. He is currently working toward the Ph.D. degree in mathematics with the School of Mathematical Sciences, University of Electronic Science and Technology of China, Chengdu, China.

His current research interests include low-rank and sparse modeling, tensor decomposition, and high-dimensional image processing.

Yong Chen received the B.S. degree in mathematics and applied mathematics from the School of Science from East China University of Technology, Nanchang, China, in 2015, and the Ph.D. degree in mathematics from the School of Mathematical Sciences, University of Electronic Science and Technology of China, Chengdu, China, in 2020.

He is currently working with the School of Computer and Information Engineering, Jiangxi Normal University, Nanchang, China. From 2018 to 2019, he was a Research Intern with the Geoinformatics unit, RIKEN Center for Advanced Intelligence Project, Japan. His research interests include remote sensing image processing and low-rank matrix/tensor representation.

Shan-Shan Xu received the B.S. degree in information and computing science from Southwest Petroleum University, Chengdu, China, in 2019. She is currently working toward the M.S. degree in mathematics with the School of Mathematical Sciences, University of Electronic Science and Technology of China, Chengdu, China.

Her research interests include remote sensing and image processing.

Ting-Zhu Huang received the B.S., M.S., and Ph.D. degrees in computational mathematics from the Department of Mathematics, Xi'an Jiaotong University, Xi'an, China.

He is currently a Professor with the School of Mathematical Sciences, University of Electronic Science and Technology of China, Chengdu, China. His current research interests include scientific computation and applications, numerical algorithms for image processing, numerical linear algebra, preconditioning technologies, and matrix analysis with applications.

Dr. Huang is an Editor of the *Scientific World Journal*, *Advances in Numerical Analysis*, the *Journal of Applied Mathematics*, the *Journal of Pure and Applied Mathematics: Advances in Applied Mathematics*, and the *Journal of Electronic Science and Technology*, China.